

## **Interdiffusion-controlled Kondo suppression of injection efficiency in metallic non-local spin valves**

L. O'Brien<sup>1,2</sup>, D. Spivak<sup>3</sup>, J. S. Jeong<sup>1</sup>, K. A. Mkhoyan<sup>1</sup>, P. A. Crowell<sup>3</sup> and C. Leighton<sup>1</sup>

<sup>1</sup> Department of Chemical Engineering and Materials Science, University of Minnesota, MN, USA.

<sup>2</sup> Thin Film Magnetism, Cavendish Laboratory, University of Cambridge, UK.

<sup>3</sup> School of Physics and Astronomy, University of Minnesota, MN, USA

**Abstract:** Non-local spin valves (NLSVs) generate pure spin currents, providing unique insight into spin injection and relaxation at the nanoscale. Recently it was shown that the puzzling low temperature non-monotonicity of the spin accumulation in all-metal NLSVs occurs due to a manifestation of the Kondo effect arising from dilute local-moment-forming impurities in the non-magnetic material. Here it is demonstrated that precise control over interdiffusion in Fe/Cu NLSVs *via* thermal annealing can induce dramatic increases in this Kondo suppression of injection efficiency, observation of injector/detector separation-dependent Kondo effects in both charge and spin channels simultaneously, and, in the limit of large interdiffusion, complete breakdown of standard Valet-Fert-based models. The Kondo effect in the charge channel enables extraction of the exact interdiffusion profile, quantifying the influence of local moment density on the injection efficiency, and presenting a well-posed challenge to theory.

Corresponding author: leighton@umn.edu

PACS No's: 72.25.Ba, 85.75-d, 72.15.Qm, 72.10.Fk

Improved understanding of spin transport in metals is important for the development of low resistance alternatives to the tunnel magnetoresistance<sup>1-4</sup> field sensors used in hard disk drive read heads and will require a substantial increase in the current knowledge of spin injection and relaxation in metals.<sup>5</sup> Because they enable separation of charge and spin currents, non-local spin valves (NLSVs)<sup>6</sup> provide critical insight into these issues, particularly at the nanoscale.<sup>7</sup> In the non-local geometry (inset, Fig. 1(b)) two ferromagnetic metal (FM) electrodes are separated by a distance  $d$ , and are connected by a non-magnetic metal (NM) channel. Controlled by the current polarization in the FM,  $\alpha_{FM} = (I_{\uparrow} - I_{\downarrow})/(I_{\uparrow} + I_{\downarrow})$ , a charge current driven from the FM injector into the NM generates a non-equilibrium spin accumulation in the NM, and a pure spin current between the two FMs. The spin imbalance decays on a length scale  $\lambda_N$ , the NM spin diffusion length, and some fraction of the spin accumulation thus persists at the FM detector. This results in a chemical potential difference between the FM detector and the NM far from the FM, which is modulated by toggling the magnetizations of the FMs between parallel and anti-parallel. The resulting non-local spin resistance,  $\Delta R_{NL} = \Delta V_{NL}/I$ , provides a direct probe of the spin accumulation, and thus  $\lambda_N$  (via  $\Delta R_{NL}(d)$ ).

Contrary to simple expectations based on Elliott-Yafet spin relaxation<sup>8-10</sup>,  $\Delta R_{NL}(T)$  is observed to be non-monotonic in many all-metal NLSVs, first increasing on cooling, but then decreasing at low  $T$ .<sup>11-17</sup> This  $T$  dependence has recently been explained as a manifestation of the Kondo effect,<sup>18,19</sup> due to dilute local-moment-forming FM impurities in the NM.<sup>20</sup> In essence, the interaction of the NM conduction electrons with impurity virtual bound states as they screen the randomly oriented FM impurity moments induces depolarization of the injected spin current around the Kondo temperature  $T_K$ . This occurs even in NM channels prepared from impurity-free source materials, due to inevitable chemical interdiffusion between the FMs and the NM at interfaces.<sup>20</sup> NM contamination due to finite source purity, or transfer of FM impurities from resists, has also been discussed,<sup>12,13</sup> with recent work<sup>21</sup> confirming previous statements<sup>20</sup> that the Kondo effect will impact  $\lambda_N$  in addition to suppressing current polarization in channels contaminated with FM impurities. As

expected, in the interdiffused case the non-monotonic behavior of  $\Delta R_{NL}(T)$  is observed only for combinations of FM and NM in which isolated impurities of the FM form local moments in the NM, and hence no peak is observed when Al is used as a NM.<sup>20</sup> Despite such progress, much remains to be understood about this effect, including the detailed mechanism causing depolarization of the spin current, and the dependence on interdiffusion, impurity concentration, *etc.*

In this work, fine control over the interdiffusion profile between FM contacts and a NM channel *via* thermal annealing of Fe/Cu NLSVs is demonstrated, enabling direct study of the relationship between the Fe impurity concentration  $C_{Fe}(x)$  in the Cu and the low  $T$  Kondo-suppression of spin accumulation. Increasing the annealing temperature ( $T_A$ ), and thus the extent of interdiffusion, is found to lead to a strong increase in Kondo-induced depolarization, and eventually to breakdown of 1-D solutions based on the Valet-Fert formalism.<sup>22,23</sup> Moreover, promoting interdiffusion out to mesoscopic length scales is shown to lead to  $d$ -dependent Kondo effects in both charge and spin channels. The  $d$  dependence of the charge Kondo effect then enables precise determination of  $C_{Fe}(x)$ , validated against STEM/EDX (scanning transmission electron microscopy / energy dispersive X-ray spectroscopy) characterization. The relation between the Fe diffusion length  $\ell_{Fe}$  and the Kondo-suppression of injection efficiency is thus obtained, providing a well-defined result with which to test future theory in this technologically and fundamentally important class of canonical spin transport devices.

Devices studied here were fabricated on Si/SiN substrates by electron-beam lithography. Multi-angle Fe and Cu electron beam evaporation (base pressure  $<10^{-9}$  Torr) through a suspended resist mask was employed to avoid intermediate air exposure.<sup>24,25</sup> Growth rates and pressures were: 0.5 Å/s,  $1 \times 10^{-9}$  Torr; and 1 Å/s,  $1 \times 10^{-8}$  Torr, for Fe and Cu, respectively, and the nominal Cu source purity was 99.999 %, *i.e.*  $C_{Fe} < 10$  ppm. Fe/Cu is chosen as illustrative because dilute quantities of Fe are both miscible and moment-forming in Cu,<sup>26,27</sup> with  $T_K = 30$  K. FM injector, FM detector, and NM channel widths and thicknesses were:  $w_{FM,inj} = 150$  nm,  $w_{FM,det} = 100$  nm,  $w_N = 150$  nm; and

$t_{FM} = 16$  nm,  $t_N = 200$  nm. The FM injector/detector separation  $d$  was varied between 150 nm and 5  $\mu$ m. Post-fabrication annealing was performed under high vacuum ( $10^{-6}$  Torr) at various  $T_A$ , for 2 hours. For structural/chemical characterization, STEM specimens were prepared using a 30 kV focused ion beam (FEI Quanta 200 3D) followed by 5 kV Ga ion milling, enabling cross-sectional imaging of NLSVs in the x-z plane (see inset, Fig. 1(b)). An aberration-corrected FEI Titan G2 60-300 STEM equipped with a Super-X EDX system was used, operating at 300 kV. The measured TEM specimen thicknesses, using low-loss EELS, were approximately 72 and 94 nm respectively for  $T_A = 80$  and 450  $^{\circ}$ C. Considering the effects of convergent beam broadening, channelling, and beam-specimen interaction gives an estimate of intrinsic interface broadening of  $< 1$  nm, significantly smaller than the observed interface widths in this study. Methods for transport measurements were reported in more detail in Ref. <sup>20</sup>. They involve AC excitation at 13 Hz with bias currents of 100  $\mu$ A.  $\Delta R_{NL}$  was independent of excitation current in the regime investigated.

Figs. 1 (a,b,c) show  $\Delta R_{NL}(d)$  at various measurement  $T$ , for both unannealed devices (a), and devices annealed at  $T_A = 450$  (b) and 500  $^{\circ}$ C (c). (In the unannealed case, the  $T_A$  quoted (80  $^{\circ}$ C) is the highest  $T$  experienced during processing). Other  $T_A$  values were measured, and will be summarized later, but the focus for now is placed on the illustrative values 80, 450 and 500  $^{\circ}$ C. The  $\Delta R_{NL}$  in unannealed devices (Fig. 1(a)) decreases with increasing  $d$ , as expected, with the non-monotonic  $T$  dependence discussed above. Specifically, at a given  $d$ ,  $\Delta R_{NL}$  first increases on cooling, before decreasing below 50 K due to the Kondo mechanism.<sup>20</sup> As  $T_A$  increases, the low  $T$  suppression of  $\Delta R_{NL}$  becomes much more apparent, particularly at small  $d$  (e.g. Fig. 1(c)). This suggests increased Kondo-suppression of  $\Delta R_{NL}$  when interdiffusion is promoted by annealing. To quantify this observation,  $\Delta R_{NL}(d)$  was fit to a standard 1-D solution to the Valet-Fert (V-F) model<sup>23</sup> for NLSVs in the transparent interface limit.<sup>22</sup> This is the limit  $R_I, R_{FM} < R_N$ , where  $R_I$  is the FM/NM contact resistance, and  $R_{FM}, R_N$  are the spin resistances,  $R_{FM} = \rho_{FM}\lambda_{FM}/w_N w_{FM}$ , and  $R_N = \rho_N\lambda_N/w_N t_N$ . Here  $\lambda_{FM}$  is the spin diffusion length in the FM, and  $\rho_N$  and  $\rho_{FM}$  are the NM / FM resistivities.

Operation in the transparent limit was verified by the magnitude (and sign) of  $R_I$  from three-terminal measurements, the non-exponential dependence of  $\Delta R_{NL}$  on  $d$ , and the existence of FM-induced dephasing in four-terminal Hanle measurements (see supplementary discussion in Ref. <sup>20</sup> for more details). In this limit:<sup>22</sup>

$$\Delta R_{NL}(d, T) = 4 \frac{\alpha_{eff}^2 R_{FM}^2}{(1 - \alpha_{eff}^2)^2 R_N} \frac{\exp(-d/\lambda_N)}{\left[1 + \frac{2R_{FM}}{(1 - \alpha_{eff}^2)R_N}\right]^2 - \exp(-2d/\lambda_N)}, \quad (1)$$

where we define  $\alpha_{eff}$  as an *effective* value of  $\alpha_{FM}$ . This is done because, at least with the fabrication methods used here, the Kondo suppression of  $\Delta R_{NL}(T)$  is determined by local moments formed by interdiffusion at the FM/NM interfaces. In Eq. 1 this near-interface effect is manifest as a low  $T$  suppression of  $\alpha_{FM}$ , rather than  $\lambda_N(T)$ . This distinguishes  $\alpha_{eff}$  from  $\alpha_{FM}$ , an intrinsic property of the FM. Additionally, at high  $T_A$  interfacial alloying is anticipated, rendering the extracted polarization a property more of the interfacial Fe-Cu alloy than pure Fe. For these reasons we also emphasize below the  $T$  dependence of  $\alpha_{eff}$ , rather than its absolute values; the latter are nevertheless discussed in the Supplementary Information. It is essential to fix as many parameters in Eq. 1 as possible. Therefore,  $\rho_N(T)$  is measured on each NLSV,  $\rho_{FM}(T)$  is measured on FM nanowires with identical dimensions and growth/annealing parameters, and all physical dimensions in Eq. 1 are determined by microscopy. This leaves  $\lambda_N$ ,  $\lambda_{FM}$ , and  $\alpha_{eff}$  as free parameters. As described earlier,<sup>20</sup> determining  $\lambda_{FM}$  from  $\rho_{FM}$  via an empirical relationship<sup>5</sup> is an effective parameter constraint, resulting in  $\lambda_{Fe} \approx 4$  nm. This leaves only  $\lambda_N$  and  $\alpha_{eff}$  as fitting parameters. Moreover, Eq. 1 reduces to a single exponential when  $d > \lambda_N$ , directly yielding  $\lambda_N$ .  $\lambda_N$  and  $\alpha_{eff}$  are thus easily separable.

The solid lines in Figs. 1(a-c) are fits to Eq. 1 with the discussed approach. For  $T_A = 80$  °C (Fig. 1(a)), good fits are obtained, highlighting the simple exponential behavior at large  $d$  and the upward deviation at low  $d$ , which is a defining characteristic of transparent interfaces. At  $T_A = 450$  and 500 °C (Figs. 1(b,c)) the high  $d$  single exponential fall-off is maintained, but with increasingly large

departures at low  $d$  and  $T$ , due to the Kondo suppression of injection efficiency. The magnitude of these departures at low  $d$  is surprising, constituting breakdown of the standard V-F model at only modest (see below) levels of FM/NM interdiffusion, highlighting the remarkable efficiency with which dilute FM impurities relax spin. This Kondo suppression is illustrated in Figs. 1(d,e) in which the extracted  $\alpha_{eff}(T)$  (normalized to its maximum,  $\alpha_{max}$ ; absolute values of  $\alpha_{eff}$  are shown in the Supplementary Information) and  $\lambda_N(T)$  are shown vs.  $T_A$ . Note that for  $T_A = 450$  and  $500$  °C, the values shown are from fits of  $\Delta R_{NL}(d)$  in the region  $d \geq 500$  nm (Figs. 1(b,c)), which must be borne in mind when considering extracted  $\alpha_{eff}$  values. In this, and all subsequent plots, we use green, blue, and red for  $T_A = 80, 450$ , and  $500$  °C, respectively. Also shown in Figs. 1(d,e) are data from an NLSV with a thin ( $\sim 5$  nm) Al interlayer (IL) between the Fe and Cu. As described in ref.<sup>20</sup>, the Al both inhibits interdiffusion and quenches local moments (Al does not support local moments on Fe impurities), eliminating the Kondo-suppression of  $\alpha_{FM}$ . The Al IL data thus show nearly monotonic increases in  $\alpha_{eff}$  and  $\lambda_N$  on cooling. Moving to the non-IL devices, at  $T_A = 80$  °C a low  $T$  downturn in  $\alpha_{eff}$  becomes more noticeable, reaching  $\sim 6$  %. At  $T_A = 450$  and  $500$  °C, however, the low  $T$  suppression is significantly increased,  $\alpha_{eff}$  decreasing by  $\sim 20$  % between 100 and 5 K. Annealing therefore promotes Fe/Cu interdiffusion, increasing  $C_{Fe}$  near the interface, and thus both the magnitude and onset  $T$  of the  $\alpha_{eff}$  suppression. This occurs in the absence of any effect in  $\lambda_N(T)$ , which saturates at low  $T$  at 400-500 nm. Note that the large error bars on  $\lambda_N$  at  $T_A = 500$  °C reflect the increased fitting error when  $\Delta R_{NL}(d)$  departs from the form of Eq. 1 (Fig. 1(c)).

A more detailed view of the dependence of  $\Delta R_{NL}(T)$  on  $d$  and  $T_A$  is provided in Fig. 2 (upper panels) where the suppression of  $\Delta R_{NL}$  below some temperature  $T_{max}$  is clear. Also shown in Fig. 2 (lower panels) are the corresponding  $\rho_N(T)$  data, plotted as  $\rho_N(T)/\rho_{min}$ , where  $\rho_{min}$  is the minimum value of  $\rho_N$ . Starting at  $T_A = 80$  °C (Fig. 2(a)), the low  $T$  suppression in  $\Delta R_{NL}$  is clearly observable, with both the magnitude ( $\sim 13$  % reduction at  $d = 250$  nm) and  $T_{max}$  ( $\sim 70$  K) comparing well to prior work.<sup>11–13,15,17,28</sup> The corresponding  $\rho_N(T)/\rho_{min}$  (Fig. 2(d)) reveals barely any indication

of the Kondo effect in charge transport (a weak minimum is actually present at  $\sim 12$  K), due to the majority of the current flowing through the low resistivity “bulk” of the NM, in which  $C_{Fe}$  is negligible.<sup>20</sup> Moving straight to the highest annealing temperature,  $T_A = 500$  °C, Figs. 2(c,f) reveal very different behavior. The Kondo suppression of  $\Delta R_{NL}$  is dramatically enhanced,  $\Delta R_{NL}(d = 250$  nm) decreasing by  $\sim 50$  % below  $T_{max} \approx 120$  K. Additionally, a clear signature of the Kondo effect emerges in the charge channel, with a minimum developing in  $\rho_N(T)$  at  $T_{min} = 18.5$  K. It is important to note here that although both effects are Kondo-derived, the  $T_{max}$  in  $\Delta R_{NL}(T)$  and the  $T_{min}$  in  $\rho_N(T)$  do not coincide with each other, or with  $T_K$  (30 K). This is because  $T_{max}$  is determined by  $\alpha_{eff}(T)$ ,  $\rho_{N,FM}(T)$  and  $\lambda_{N,FM}(T)$ , whereas  $T_{min}$  is controlled by the relative contributions of phonon and Kondo scattering to  $\rho_N(T)$ . Nonetheless, it is clear from Figs. 2(c,f) that 500 °C annealing promotes interdiffusion to such a degree that significant  $C_{Fe}$  occurs throughout the NM (note the  $d$ -independence in Fig. 2(f)), inducing large Kondo effects in both spin ( $\Delta R_{NL}$ , Fig. 2(c)) and charge transport ( $\rho_N$ , Fig. 2(f)). The most interesting result, however, is obtained at the intermediate annealing temperature,  $T_A = 450$  °C (Figs. 2(b,e)). Here the maximum in  $\Delta R_{NL}$  and minimum in  $\rho_N(T)$  are of course intermediate between  $T_A = 80$  and 500 °C, but  $\rho_N(T)/\rho_{min}$  is also now *strongly*  $d$ -dependent (Fig. 2(e)). Both  $T_{min}$  and the strength of the Kondo minimum increase as  $d$  decreases, indicating that at  $T_A = 450$  °C a clear gradient in  $C_{Fe}(x)$  occurs along the NM channel, resulting in a  $d$ -dependent strength of the Kondo effect. This concentration gradient is illustrated by the color gradient in the inset to Fig. 1(b). Note that from Fig. 2 it appears that increasing annealing temperature from 80 to 450 °C increases  $\Delta R_{NL}(d, T)$ . Care must be taken, however, as variations in FM and NM dimensions (between samples), or  $\rho_N$ ,  $R_I$ ,  $\lambda_{FM}$  or  $\alpha_{FM}$  (with annealing) can cause systematic differences in  $\Delta R_{NL}(d, T)$ .

Importantly, the  $\rho_N(T)$  data shown in Figs. 2(d-f) enable, in conjunction with established knowledge of the conventional Kondo effect for Fe in Cu, extraction of the average value  $\langle C_{Fe} \rangle$  of  $C_{Fe}$  in the NM as a function of  $d$  and  $T_A$ . To do this,  $\rho_N(T)$  around  $T_{min}$  is fit to the simple form:<sup>29</sup>

$$\rho_N(T) = \rho_0 + AT^5 - \rho_K \log T, \quad (2)$$

where  $\rho_0$  accounts for  $T$ -independent impurity scattering, the  $AT^5$  term for phonon scattering, and the  $\rho_K$  term for the charge Kondo effect. Because  $\rho_K \propto \langle C_{Fe} \rangle$ , in this simple case then  $T_{min} = \eta \langle C_{Fe} \rangle^{1/5}$ ,<sup>30</sup> where  $\eta$  is a constant known from prior work<sup>31</sup> (8.07 K with  $\langle C_{Fe} \rangle$  in ppm). Fitting the data of Figs. 2(d-f) with Eq. 2 yields the  $T_{min}(d)$  data shown in Fig. 3(a). Note the relatively high,  $d$ -independent  $T_{min}$  at  $T_A = 500$  °C, and the strongly  $d$ -dependent  $T_{min}$  at  $T_A = 450$  °C. These  $T_{min}(d)$  data can then be converted to  $\langle C_{Fe}(d) \rangle$  [Fig. 3(b)], from which it is clear that the  $T_A$  range investigated encompasses three regimes. At low  $T_A$  (80 °C) interdiffusion is limited to the near interface region. Only a trace concentration of Fe is detected in the bulk of the NM ( $\sim 7$  ppm), in line with the nominal Cu source purity. At intermediate  $T_A$  (450 °C) substantial interdiffusion occurs, over mesoscopic scales, resulting in a  $d$ -dependent  $\langle C_{Fe} \rangle$ . In essence the diffusion length for Fe into Cu at  $T_A = 450$  °C becomes comparable to the  $d$  range probed (100's of nm). Finally, at high  $T_A$  (500 °C), the diffusion length significantly exceeds the probed  $d$  range, and  $\langle C_{Fe} \rangle$  assumes a relatively large,  $d$ -independent value ( $\sim 63$  ppm). Qualitatively this behavior is consistent with expectations for thermally activated interdiffusion in polycrystalline metals, where diffusion occurs both *via* grain (G) and grain boundary (GB) mechanisms.<sup>32,33</sup> These have characteristic activation energies ( $Q_G, Q_{GB}$ ) and diffusion lengths ( $\ell_{Fe}^G(T_A), \ell_{Fe}^{GB}(T_A)$ ) which, as discussed in full in Supplementary Information, can simply explain the behavior in Fig. 3(b). In particular, the rapid onset of interdiffusion above  $T_A = 400$  °C is easily understood: As  $Q_{GB}$  is overcome at high  $T_A$ , grain boundary diffusion offers a short circuit to uniform 'doping' of the NM. It is noted: (a) that the Kondo effect in charge transport is one of the few ways one could imagine quantifying the ppm-level chemical profile in these exact devices, and that (b) the comparison of  $\Delta R_{NL}(d, T)$  and  $\rho_N(d, T)$  in Fig. 2, and the above analysis, clearly illustrates which parameters set  $T_{max}$  and  $T_{min}$ , expanding our understanding over Ref. 20.

To quantify the above statements regarding diffusion mechanisms, and directly probe  $\ell_{Fe}$  in these devices, STEM/EDX was performed. Figs. 3(c,d) show representative cross-sectional EDX maps



of Fe, Cu and Si (in the  $x$ - $z$  plane, as indicated in the inset to Fig. 1(b)) of Fe/Cu NLSVs annealed at 80 and 450 °C. Not only are the Fe injector/detector, Cu channel, and Si substrate clearly observed, but it is also seen that the Fe/Cu interface is significantly interdiffused for  $T_A = 450$  °C (Fig. 3(d)). Due to asymmetry in the in-plane vs. out-of-plane grain dimensions, and so the weighting of G to GB diffusion,  $\ell_{Fe}$  is somewhat anisotropic (Figs. 3(c,d)). Despite this asymmetry, in-plane and out-of-plane  $\ell_{Fe}$  values scale similarly with  $T_A$ . Moreover, the interdiffusion of Fe through the Cu channel will be determined by the in-plane  $\ell_{Fe}$ , due to the relative scale of the channel length ( $\mu\text{m}$ 's) and width (200 nm), compared to the channel height (200 nm). As such, only the in-plane value of  $\ell_{Fe}$  is discussed here. Figs. 3(e,f) show line scans of the in-plane  $C_{Fe}(x)$  through the FM, surrounded by NM. The solid lines in Figs. 3(e,f) are fits to a 1-D semi-infinite diffusion profile at each interface,  $C_{Fe} \propto 1 - \text{erf}(x/\ell_{Fe})$ , resulting in  $\ell_{Fe} = 4.5$  nm at  $T_A = 80$  °C, increasing four-fold to 16.3 nm at  $T_A = 450$  °C. Such measurements of course only probe  $C_{Fe}$  in the interface region, being insensitive to the sub-100 ppm tails of the interdiffusion profile relevant to Kondo physics. To determine  $\ell_{Fe}$  further from the FM/NM interfaces,  $\langle C_{Fe} \rangle$  from Fig. 3(b) was also fit with a 1-D semi-infinite slab diffusion approach ( $C_{Fe} \propto 1 - \text{erf}(x/\ell_{Fe})$ ), accounting for the finite solubility of Fe in Cu<sup>34</sup> using

$$\langle C_{Fe}(d) \rangle = \frac{1}{d - 2d_0} \int_{d_0}^{d-d_0} C_{Fe} dx, \quad (3)$$

with  $d_0$  being the distance from the FM contact at which the bulk solubility limit of Fe in Cu is reached (see Supplementary Information for a full discussion). By considering only the near-interface region beyond the solubility limit of Fe in Cu, we intentionally characterize the dilute regime of interdiffusion appropriate to the Kondo effect alone. The solid blue line in Fig. 3(b) shows the result of such fitting. The data are well described with  $\ell_{Fe}(T_A = 450 \text{ °C}) = 12.4$  nm, in very reasonable agreement with the 16.3 nm obtained from EDX. The near interface EDX concentration is thus consistent with the ppm-level tail from analysis of the charge Kondo effect.

The right axis of Fig. 3(g) shows  $\ell_{Fe}(T_A)$  determined *via* these two methods, *i.e.* EDX (open squares) and the charge Kondo effect (open triangle). Significantly, the solid line through the data is a fit to the two-channel 1-D model (G and GB diffusion) described in detail in Supplementary Information. The fit describes the data well, with  $Q_{GB}/Q_B = 0.7$ , and an  $\ell_0$  (the unannealed Fe interdiffusion length) of 5.3 nm. Both values are entirely reasonable,  $Q_{GB}/Q_B$  being consistent with literature values,<sup>33</sup> while  $\ell_0$  lies close to the unannealed EDX result (4.5 nm). On the left axis of Fig. 3(g), the  $T_A$  dependence of  $\ell_{Fe}$  is then compared to  $\alpha_{eff}(T = 5\text{ K})/\alpha_{max}$ . The dashed line is a guide to the eye, while the red circle is  $\alpha_{eff}(T = 5\text{ K})$  for the Al IL device, for which the Kondo suppression is negligible. These compiled data (which include numerous  $T_A$  values in addition to the 80, 450 and 500 °C discussed thus far), reveal that only weak interdiffusion occurs below  $T_A \approx 300\text{ °C}$  (dotted line), with commensurately modest impact on  $\alpha_{eff}$ . An annealing effect is nevertheless noticeable, and clearly impacts  $\Delta R_{NL}$  (see ref. 20 and Figs. 1(a,d) and 2(a)). Above about 300 °C, however, interdiffusion turns on rapidly, resulting in 10's of ppm  $\langle C_{Fe} \rangle$  values, strong Kondo effects in both charge and spin transport, and a large decrease in the low  $T$  value of  $\alpha_{eff}$ . In general, relating the Kondo suppression of spin polarization (which is not yet on a firm theoretical footing), with a concentration profile across an FM/NM interface, and into the NM, is a non-trivial exercise. A plot of the type shown in Fig 3(g), however, reduces the problem to comparing only two independent parameters: The suppression in effective injection efficiency and the interdiffusion length. Quantifying the  $\ell_{Fe}$ - $\alpha_{eff}$  relation in this manner thus provides a compact summary of the influence of the FM/NM interface chemical profile on the Kondo-suppressed spin polarization in NLSVs, posing a well-defined challenge to future theoretical treatments of spin relaxation *via* the Kondo effect. More broadly, this method of correlating both spin and charge transport with chemical and structural characterization provides a precise means to isolate and determine the mechanisms limiting spin diffusion in metals.

Acknowledgments: This work was funded by Seagate Technology Inc., the University of Minnesota (UMN) NSF MRSEC under awards DMR-0819885 and DMR-1420013, and DMR-1507048. L.O'B. acknowledges a Marie Curie International Outgoing Fellowship within the 7<sup>th</sup> European Community Framework Programme (project no. 299376). Parts of this work were carried out in the UMN Characterization Facility and Minnesota Nano Center, which receive partial support from the NSF MRSEC and NSF NNIN programs, respectively. We thank David Deen of Seagate for productive conversations.

## References

- <sup>1</sup> M. Julliere, Phys. Lett. A **54**, 225 (1975).
- <sup>2</sup> J.S. Moodera, L.R. Kinder, T.M. Wong, and R. Meservey, Phys. Rev. Lett. **74**, 3273 (1995).
- <sup>3</sup> S. Yuasa, T. Nagahama, A. Fukushima, Y. Suzuki, and K. Ando, Nat. Mater. **3**, 868 (2004).
- <sup>4</sup> S.S.P. Parkin, C. Kaiser, A. Panchula, P.M. Rice, B. Hughes, M. Samant, and S.-H. Yang, Nat. Mater. **3**, 862 (2004).
- <sup>5</sup> J. Bass and W.P. Pratt, J. Phys. Condens. Matter **19**, 183201 (2007).
- <sup>6</sup> M. Johnson and R.H. Silsbee, Phys. Rev. Lett. **55**, 1790 (1985).
- <sup>7</sup> F.J. Jedema, A.T. Filip, and B.J. van Wees, Nature **410**, 345 (2001).
- <sup>8</sup> R.J. Elliott, Phys. Rev. **96**, 266 (1954).
- <sup>9</sup> F. Beuneu and P. Monod, Phys. Rev. B **18**, 2422 (1978).
- <sup>10</sup> P. Monod and F. Beuneu, Phys. Rev. B **19**, 911 (1979).
- <sup>11</sup> T. Kimura, T. Sato, and Y. Otani, Phys. Rev. Lett. **100**, 066602 (2008).
- <sup>12</sup> E. Villamor, M. Isasa, L.E. Hueso, and F. Casanova, Phys. Rev. B **87**, 094417 (2013).
- <sup>13</sup> H. Zou and Y. Ji, Appl. Phys. Lett. **101**, 082401 (2012).
- <sup>14</sup> Y. Otani and T. Kimura, Philos. Trans. A. Math. Phys. Eng. Sci. **369**, 3136 (2011).
- <sup>15</sup> M. Erekhinsky, F. Casanova, I.K. Schuller, and A. Sharoni, Appl. Phys. Lett. **100**, 212401 (2012).
- <sup>16</sup> F. Casanova, A. Sharoni, M. Erekhinsky, and I. Schuller, Phys. Rev. B **79**, 184415 (2009).
- <sup>17</sup> T. Kimura, N. Hashimoto, S. Yamada, M. Miyao, and K. Hamaya, NPG Asia Mater. **4**, e9 (2012).
- <sup>18</sup> J. Kondo, Prog. Theor. Phys. **32**, 37 (1964).
- <sup>19</sup> J. Kondo, *The Physics of Dilute Magnetic Alloys* (Cambridge University Press, Cambridge, 2012).
- <sup>20</sup> L. O'Brien, M.J. Erickson, D. Spivak, H. Ambaye, R.J. Goyette, V. Lauter, P.A. Crowell, and C. Leighton, Nat. Commun. **5**, 3927 (2014).
- <sup>21</sup> J.T. Batley, M.C. Rosamond, M. Ali, E.H. Linfield, G. Burnell and B.J. Hickey, arXiv:1504.07515 (2015)
- <sup>22</sup> S. Takahashi and S. Maekawa, Phys. Rev. B **67**, 052409 (2003).
- <sup>23</sup> T. Valet and A. Fert, Phys. Rev. B **48**, 7099 (1993).

- <sup>24</sup> F.J. Jedema, M. V. Costache, H.B. Heersche, J.J.A. Baselmans, and B.J. van Wees, Appl. Phys. Lett. **81**, 5162 (2002).
- <sup>25</sup> Y. Ji, A. Hoffmann, J.S. Jiang, J.E. Pearson, and S.D. Bader, J. Phys. D: Appl. Phys. **40**, 1280 (2007).
- <sup>26</sup> J.A. Mydosh, *Spin Glasses: An Experimental Introduction* (Taylor & Francis, London, 1993).
- <sup>27</sup> M. Daybell and W. Steyert, Phys. Rev. **167**, 536 (1968).
- <sup>28</sup> M. Erekhinsky, A. Sharoni, F. Casanova, and I.K. Schuller, Appl. Phys. Lett. **96**, 022513 (2010).
- <sup>29</sup> For these devices,  $T_{min} \sim T_K \ll T_D$  (the Debye temperature). As  $\rho_N(T)$  is fit near the Kondo minimum, contributions from both the full phenomenological expression (ref. 35) of the Kondo effect, and Debye model of phonon scattering may be approximated by equation 2.
- <sup>30</sup> This is obtained simply using,  $\frac{\partial \rho_N}{\partial T} |_{T=T_{min}} = 0 = 5AT_{min}^4 - \frac{\rho_K}{T_{min}}$ , which then yields 
$$T_{min} = \left( \frac{\rho_K}{5A} \right)^{1/5}.$$
- <sup>31</sup> J.P. Franck, F.D. Manchester, and D.L. Martin, Proc. R. Soc. A **263**, 494 (1961).
- <sup>32</sup> J.C. Fisher, J. Appl. Phys. **22**, 74 (1951).
- <sup>33</sup> Y. Mishin and C. Herzig, Mater. Sci. Eng. A **260**, 55 (1999).
- <sup>34</sup> T. Hutchison and J. Reekie, Phys. Rev. **83**, 854 (1951).
- <sup>35</sup> D. Goldhaber-Gordon, J. Göres, M. Kastner, H. Shtrikman, D. Mahalu, and U. Meirav, Phys. Rev. Lett. **81**, 5225 (1998).

## Figures

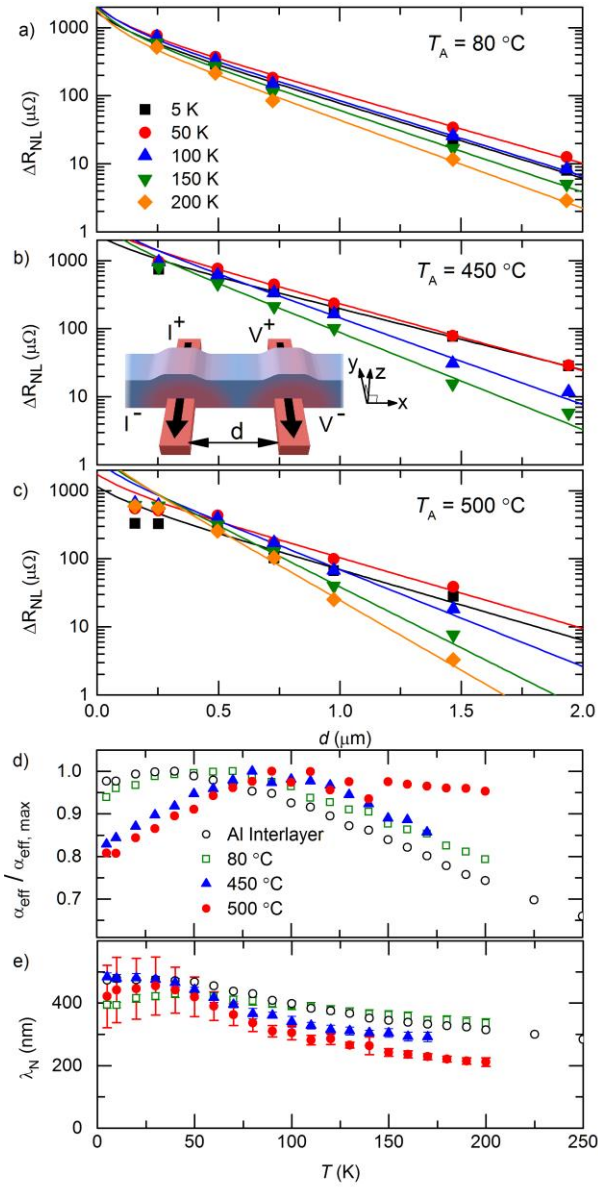


**Figure 1.**  $d$ -dependence of  $\Delta R_{NL}$  at 5, 50, 100, 150, and 200 K, for devices annealed at  $T_A = 80^\circ\text{C}$  (a),  $450^\circ\text{C}$  (b) and  $500^\circ\text{C}$  (c). Solid lines are fits to equation 1. The inset to (b) is a schematic, depicting an NLSV with FM/NM interdiffusion.  $T$  dependence of (d)  $\alpha_{eff}$ , normalized to its maximum, as extracted from fits to  $\Delta R_{NL}(d, T)$ , and (e) the corresponding  $\lambda_N$ . Data are shown for devices with a 5 nm Al interlayer, and devices annealed at  $T_A = 80, 450$ , and  $500^\circ\text{C}$ .

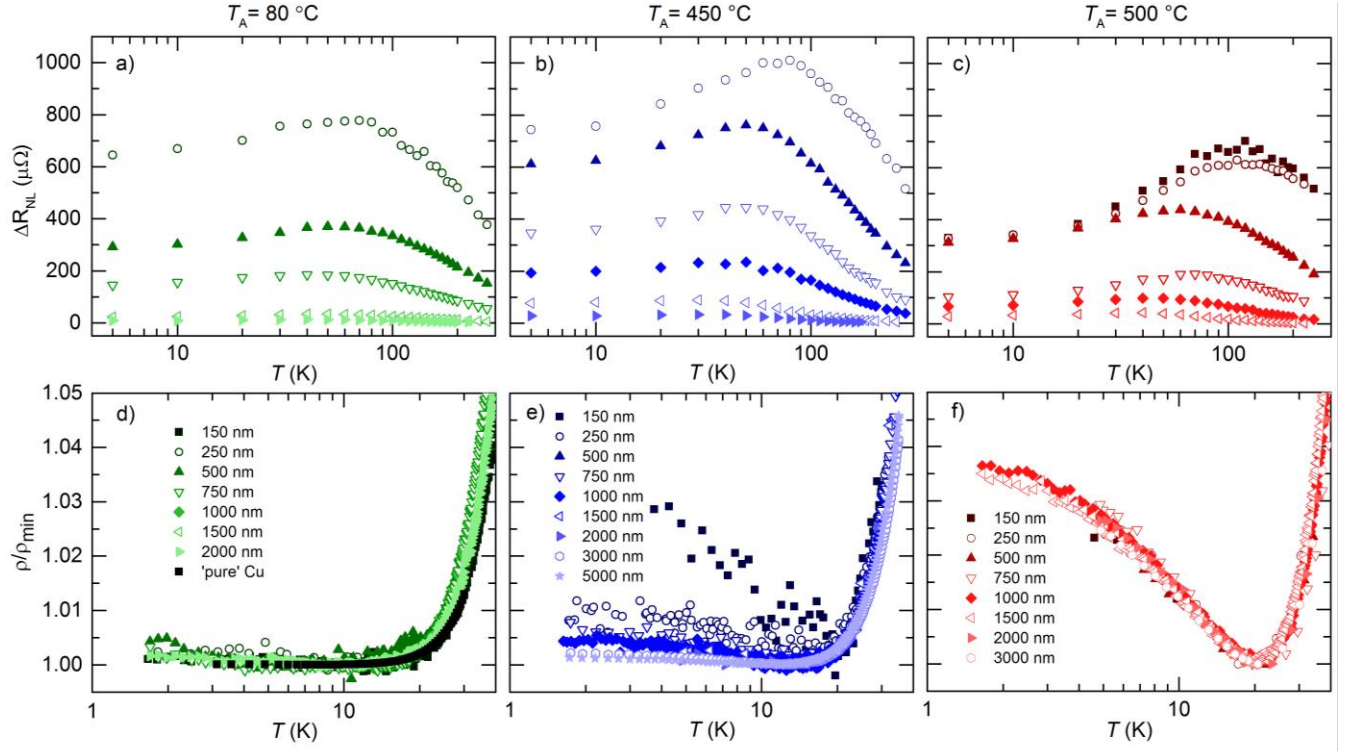


**Figure 2.**  $\Delta R_{NL}(T)$ , for various  $d$ , for  $T_A = 80$  °C (a), 450 °C (b) and 500 °C (c). (d,e,f) Corresponding low temperature  $\rho_N(T)/\rho_{min}$ . Note the logarithmic  $T$  axes, with different scales for  $\Delta R_{NL}(T)$  and  $\rho_N(T)$ .

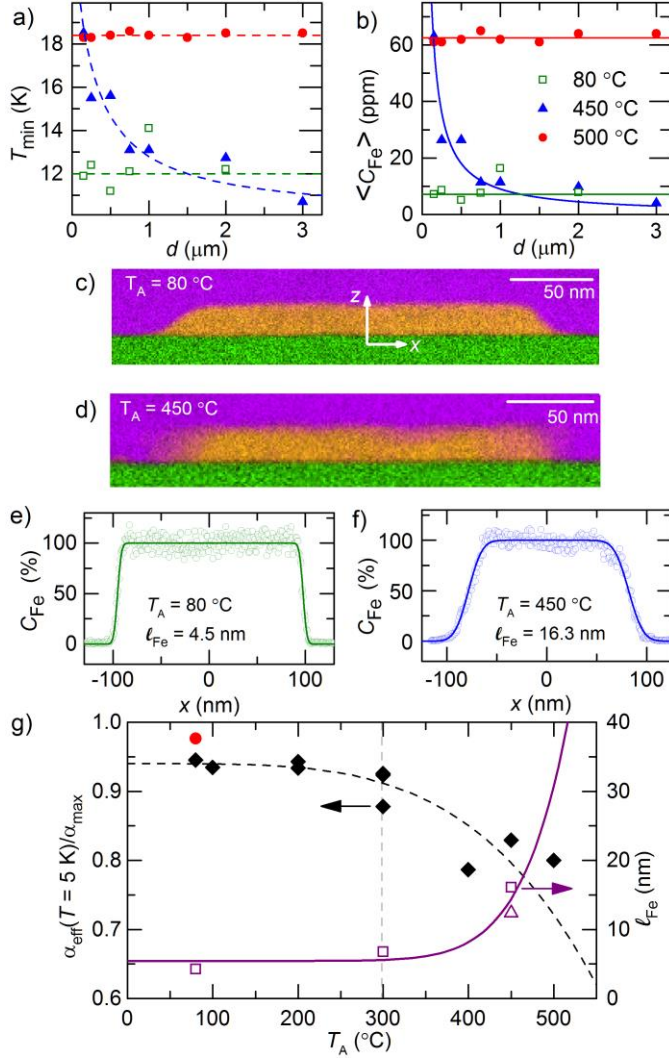


**Figure 3.** (a)  $d$ -dependence of  $T_{min}$  for  $T_A = 80, 450$ , and  $500$  °C. Dashed lines are guides to the eye. (b)  $d$ -dependence of  $\langle C_{Fe} \rangle$  from  $T_{min} = \eta \langle C_{Fe} \rangle^{1/5}$ , with  $\eta = 8.07$  K. Solid lines are fits based on constant concentration (80 and 500 °C) or a semi-infinite-medium interdiffusion model (450 °C anneal,  $\ell_{Fe} = 12.4$  nm). (c,d) STEM/EDX maps (purple, Cu; orange, Fe; green, Si) at  $T_A = 80$  and  $450$  °C. (e,f) Lateral EDX line scans of  $C_{Fe}(x)$  (open circles); the solid lines are fits to a semi-infinite-medium diffusion model. (g)  $\alpha_{eff}(T = 5 \text{ K})/\alpha_{max}$ , normalized to  $\alpha_{max}$ , as a function of  $T_A$  (black diamonds, left axis). The red circle indicates an Fe/Al IL/Cu device. The open purple data (right axis) show  $\ell_{Fe}(T_A)$  from Kondo (triangle) and STEM/EDX (squares) analyses. The solid purple line is a fit to a two-channel interdiffusion model.